Research Square

Preprints are preliminary reports that have not undergone peer review.
They should not be considered conclusive, used to inform clinical practice,
or referenced by the media as validated information.

Acoustic Cluster Therapy (ACT) and delivery of polymeric micelles: The impact of drug properties and microenvironment in pancreatic tumours

Jessica Lage Fernandez
Norwegian University of Science and Technology
Melina Mühlenpfordt
Norwegian University of Science and Technology
Charlotte Årseth
Norwegian University of Science and Technology
Sofie Snipstad
Norwegian University of Science and Technology
Einar Sulheim
Norwegian University of Science and Technology
Annemieke van Wamel
Norwegian University of Science and Technology
Sverre H. Torp
Norwegian University of Science and Technology
Cristianne J.F. Rijcken
Cristal Therapeutics
Qizhi Hu
Cristal Therapeutics
Marielle Thewissen
Cristal Therapeutics
Catharina de Lange Davies
catharina.davies@ntnu.no
Norwegian University of Science and Technology

Article

Keywords: Ultrasound, microbubbles, nanoparticles, tumour uptake, microenvironment, collagen

Posted Date: November 27th, 2026

DOI: https://doi.org/10.21203/rs.3.rs-11688424/v1

License: This work is licensed under a Creative Commons Attribution 4.0 International License.
Read Full License

Additional Declarations: No competing interests reported.

Acoustic Cluster Therapy (ACT) and delivery of polymeric micelles: The impact of drug properties and microenvironment in pancreatic tumours.

Jessica Lage Fernandez[1], Melina Mühlenpfordt[1,4], Charlotte Årseth[1], Sofie Snipstad[1,6], Einar Sulheim[1,4], Annemieke van Wamel[1], Sverre H. Torp[2,3], Cristianne J.F. Rijcken[5], Qizhi Hu[5], Marielle Thewissen[5], and Catharina de Lange Davies[1*]

[1] Department of Physics, Norwegian University of Science and Technology, Trondheim, Norway
[2] Department of Clinical and Molecular Medicine, Norwegian University of Science and Technology, Trondheim, Norway
[3] Department of Pathology, St. Olavs Hospital, Trondheim University Hospital, Trondheim, Norway
[4] Exact Therapeutics, Oslo, Norway
[5] Cristal Therapeutics, Maastricht, The Netherlands
[6] Cancer Clinic, St. Olavs Hospital, Trondheim, Norway
* Corresponding author

Abstract

Treatment of pancreatic ductal adenocarcinoma (PDAC) represents a therapeutic challenge due to chemoresistance and limited delivery of drugs caused by poor perfusion and a dense extracellular matrix. Therefore, new strategies are needed to treat PDAC. We investigated the effect of Acoustic Cluster Therapy (ACT), an ultrasound-mediated drug delivery technology, on the accumulation of two cargos with distinct physicochemical properties, core-crosslinked polymeric micelles (CCPM) and a macromolecule tracer (IRDye800CW-PEG) in a murine PDAC model, the KPC model. The accumulation of IRDye800CW-PEG and CCPM was imaged in a small animal optical scanner, and the microdistribution of the micelles was imaged by confocal laser scanning microscopy. ACT increased the tumour uptake of IRDye800CW-PEG 1.5-fold, but did not significantly enhance accumulation of the micelles. CCPM exhibited substantial tumour uptake and intratumoral distribution in both control and ACT tumours, suggesting efficient tumour delivery independent of ACT. A variation in CCPM accumulation was observed. To identify tumour microenvironment characteristics that could explain the variation, functional vessels, collagen content and organisation were investigated. Among these factors, the organisation of the fibrillar collagen network had a pronounced influence on CCPM uptake. Accumulation of CCPM increased with increasing alignment of collagen fibres measured by the second-harmonic signal. These findings highlight the importance of considering both the physicochemical properties of the therapeutic agent and the structure of the collagen network to achieve successful delivery.

Key word: Ultrasound, microbubbles, nanoparticles, tumour uptake, microenvironment, collagen

Introduction

Sufficient delivery of therapeutic agents is key to effective treatment of solid tumours. However, the delivery of systemically administered therapeutics is often impaired by insufficient extravasation and limited penetration through the extracellular matrix due to endothelial, stromal and cellular barriers [1-3].

Pancreatic ductal adenocarcinoma (PDAC) is one of the most aggressive solid tumours, with low survival rate [4]. PDAC is characterized by a poorly developed vascular network and extensive desmoplasia. The increased production of extracellular matrix components such as collagen, fibronectin and hyaluronan form the dense desmoplasia which enhances the interstitial fluid pressure and compresses blood vessels, all factors limiting the delivery of therapeutics [5, 6]. Encapsulating drugs in nanoparticles (NPs), utilising the enhanced permeability and retention (EPR) effect, has for some tumour types demonstrated promising therapeutic results. However, the EPR effect greatly depends on tumour type and NP properties. In PDAC, the vascular permeability varies between PDAC models [7].

Core-crosslinked polymeric micelles (CCPM) [8] have emerged as a promising nanomedicine to improve the therapeutic efficacy of a range of drugs [9]. The CCPM used in this study known as CriPec®, is composed of biodegradable CCPM with active pharmaceutical ingredients covalently entrapped via hydrolysable linkers. The CCPM are small (diameter 40-100 nm), have a long circulation time (typical half-life of elimination is 16 hr in rats), high *in vivo* stability, and can be tailored with respect to drug release kinetics [10]. Preclinical evaluation has shown excellent pharmacokinetics, improving target tissue accumulation and efficacy for various drugs, including docetaxel and dexamethasone [11]. CCPM-docetaxel demonstrated prolonged systemic circulation, an improved safety profile and 4-fold enhanced tumour accumulation in patients with advanced solid tumours [12].

Although the CCPM demonstrate good therapeutic efficacy, in general less than 1 % of injected NPs accumulate in tumours [13] and even less end up inside tumour cells [14]. Ultrasound focused on the tumour in combination with circulating microbubbles has been shown to enhance the delivery of drugs and NPs and improve therapeutic response both preclinically [15-19] and clinically [20-22]. In most studies, microbubbles designed as contrast agents for ultrasound imaging are used. Acoustic Cluster Therapy (ACT) is specifically engineered for drug delivery. ACT is based on microclusters consisting of commercially available negatively charged microbubbles (Sonazoid, GE Healthcare) and an emulsion of positively charged microdroplets. Intravenously injected microclusters are activated by localised insonation at the target site. The application of low-intensity ultrasound leads to a transfer of energy from the microbubbles to the attached microdroplets, causing an instant vaporisation of the microdroplets, which form large ACT bubbles (~25 μm in diameter), called the activation step [23, 24]. The intravenously injected microclusters are free-floating, whereas ACT bubbles are deposited in a small fraction of the microvasculature of the target tissue. A major advantage of the ACT bubbles, compared to conventional ultrasound contrast agents with a diameter of typically 3-5 μm, is their 100-500 times larger volume, resulting in contact with a larger part of the capillary wall [24]. A subsequent ultrasound insonation induces controlled volume oscillations of the ACT bubbles, which result in shear stress and other biomechanical effects

on the endothelium (the enhancement step), enhancing extravasation across the capillary wall and facilitating the transport of co-administered drugs or drug-loaded NPs through the extracellular matrix. Intravital microscopy previously revealed that ACT-induced extravasation of macromolecules was either slow or fast, probably caused by diffusion or convection, respectively [25, 26]. Proof of concept studies showed an enhanced therapeutic efficacy of the drug nab-paclitaxel when combined with ACT in subcutaneously growing prostate tumours [27], of liposomal doxorubicin (Doxil) in orthotopic breast tumours [28], and in patient-derived PDAC xenografts treated with nab-paclitaxel /Gemcitabine and ACT [29].

In the present study, we investigated the effect of ACT on the accumulation of two cargos with distinct physicochemical properties, CCPM and the macromolecule tracer IRDye800CW-PEG in a murine model of pancreatic cancer. Tumour uptake showed considerable variability, particularly for CCPM, in both untreated and ACT tumours. To better understand the factors influencing the delivery of therapeutic agents, tumour characteristics such as vascularization and collagen network were examined. A well-developed vascular network is essential for distribution of the microclusters and ACT bubbles, and the amount and organization of collagen fibres influence the diffusion of NPs through the extracellular matrix [30] . Thus, we hypothesized that particularly collagen content and organization underline the heterogenous response to ACT-mediated delivery of therapeutic agents.

Material and Methods

Mice

Female albino B6 mice, purchased at 6-8 weeks of age (Janvier Labs), were housed in individually ventilated cages under conditions free of specific pathogens. Cages were enriched with housing, nesting material, and gnaw sticks and kept in a controlled environment (20-23°C, humidity of 50-60 %) at a 12-hour night/day cycle. Animals had free access to food and sterile water. All experimental procedures were performed in accordance with regulations by the National animal ethics committee named the Norwegian Food Safety Authority (in Norwegian Mattilsynet), who approved the application (ID FOTS15223), and the experimental procedure also followed the recommendation by the Federation of European Laboratory Animal Association (FELASA).

all experiments were performed in accordance with relevant named guidelines and regulations.

Cell culture and tumour cell inoculation in mice

Murine pancreatic ductal adenocarcinoma cells (KPC001S gLuc/green fluorescence protein, a kind gift from Steele Laboratories, Harvard University, USA) were cultured in Dulbecco's modified Eagle's medium (DMEM) (Gibco Invitrogen) supplemented with 10% foetal bovine serum and 1 % Penicillin Streptomycin (Sigma Aldrich). The cells were maintained in exponential growth phase at 37 °C and 5 % CO_2. Subcutaneous tumours were established by injecting $2x10^5$ cells in 20 µl DMEM into the hind limb of mice under anaesthesia using 2-3 % isoflurane (Baxter). Tumour growth was assessed by calliper measurements twice weekly. Animals with an average tumour volume of 260 mm^3 were included.

CCPM and IRDye800CW-PEG

The CCPM were manufactured and kindly provided by Cristal Therapeutics. The polymeric micelles were dual-labelled. The near-infrared fluorophore Cy7 was used to image tumour accumulation of the CCPM using a Near Infrared Fluorescence (NIRF) imaging system (IVIS® Spectrum in vivo imaging system, Perkin Elmer), and rhodamine B was used to study the microdistribution of CCPM by confocal laser scanning microscopy (CLSM) in tumour tissue sections. In brief, first, rhodamine B was conjugated to a fraction (6.6 mol %) of the lactate side chains of methacrylated $mPEG_{5000}$-*b*-$pHPMAmLac_n$ (n=1 or 2) block copolymer (22 kDa) via Steglich esterification to obtain rhodamine-labelled block copolymers. Next, fluorophore-labelled CCPM were manufactured essentially following the protocol reported previously[11, 31], except that a mixture of azide-functionalised (5 mol %), rhodamine-labelled (33 mol %) and non-functionalised (62 mol %) methacrylated $mPEG_{5000}$-*b*-$pHPMAmLac_n$ (n=1 or 2) block copolymers (22 kDa) was used to form azide-functionalised rhodamine-labelled CCPM prior to Cy7 conjugation. Analytical characterisations revealed that the obtained Cy7, rhodamine-labelled CCPM (88 mg/mL polymer, 40 μM Cy7 equiv. and 9 mM rhodamine equiv.) has a hydrodynamic size of 65 nm, with free rhodamine dye and free Cy7 label less than 1 mol % relative to that covalently attached to CCPM. The zeta-potential has previously been measured and reported to be between -0.2 mV and 0 mV [10].

The vascular contrast agent IRDye 800CW-PEG (approximately 45 kDa and diameter 12 nm; LI-COR) was used as a macromolecule tracer to study tumour uptake. The Zetapotential was measured using Zetazeiser NanoZs (Malvern Panalytical). IRDye 800CW-PEG was dissolved in 1.5 ml PBS and diluted 10x in PBS. The zetapotential was in the range -11 to -16 mV.

Acoustic Cluster Therapy (ACT)

The ACT microbubble-microdroplet cluster dispersion (PS101) was provided by EXACT Therapeutics. The ACT dispersion of microbubble-microdroplet clusters was made by reconstituting a freeze-dried suspension of microbubbles of perfluorobutane (Sonazoid Powder for Injection, 16 μL/vial) with a microdroplet emulsion of perfluoromethylcyclopentane (PFMCP, 6.8 mg/mL), dispersed in 5mM tris(hydroxymethyl)aminomethane (TRIS) buffer to form a 2 mL dispersion [24, 32]. The Sonazoid were supplied by GE Healthcare. The microbubbles are stabilized by a monomolecular phospholipid membrane of hydrogenated egg phosphatidylserine (H-EPS), which is negatively charged and embedded in an amorphous sucrose structure. The microdroplets are stabilized by monomolecular distearoylphosphatidylcholine (DSPC) phospholipid membrane containing 3 % (mol/mol) stearyl amine, resulting in an overall positive surface charge. The microbubble/microdroplet clusters have a median diameter of 4.5 μm [24].

Ultrasound set-up

A custom-built dual-frequency transducer, which utilises the fundamental (0.5 MHz) and fifth harmonic (2.7 MHz) frequency was mounted on top of a custom-made cone filled with degassed water (Figure 1) [33]. The transducer had a diameter of 42 mm, and 220 mm from the transducer surface, the -3 dB width of the beam profile was 16 and 6 mm, for 0.5 MHz and 2.7

MHz, respectively. Signals were generated with a signal generator (33500B, Agilent Technologies) and amplified with a 50 dB RF amplifier (2100L, E&I). The amplifier was connected to a switch box, which contained two electrical circuits for the electrical matching of both frequencies and switching between the two electrical configurations was achieved with a rotary switch. The bottom of the cone was covered with an optically and acoustically transparent plastic foil forming a bag. The animal was positioned in a dorsal position on top of an acoustically absorbing material (Aptflex F28, Precision Acoustics), with ultrasound gel for coupling between the acoustic absorber, the animal leg and the acoustically transparent foil.

The transducer was characterised in a water tank measurement system (Onda AIMS-III), and the pressure and -3 dB beam width were measured with a calibrated HGL-0200 hydrophone (Onda Corporation) using the AH-2010 preamplifier.

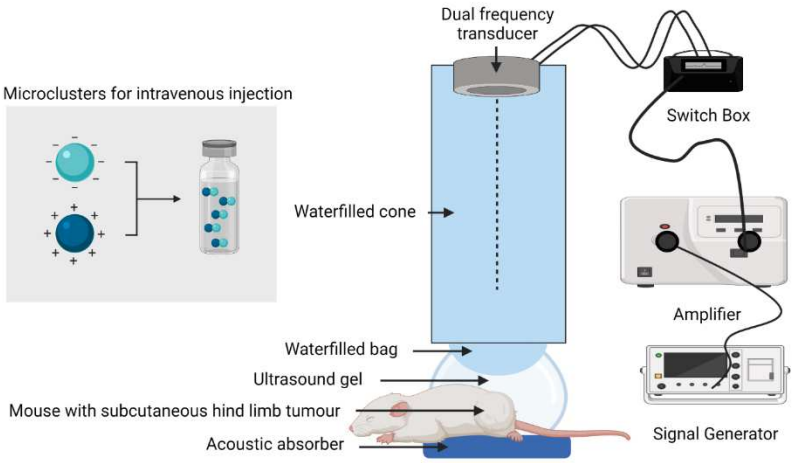

Figure 1. Illustration of microclusters to be injected intravenously and the ultrasound setup (not to scale). Mice with subcutaneously growing tumours on the hind limb are placed in prone position on the acoustic absorber, and the tumour is covered with ultrasound gel. The ultrasound transducer is placed 22 cm away from the tumours. The switch box changed between the two frequencies.

Experimental protocol

The treatment and imaging timeline for CCPM is shown in Figure 2. The timeline for IRDye800CW-PEG was similar, except that the mice were euthanized 2 hr after ACT. Two days prior to ACT, the fur was removed from the tumour-bearing leg and control leg using an electric trimmer and depilatory lotion. On the day of the intervention, mice were anaesthetised using 2-3 % isoflurane (Baxter). Anaesthesia was maintained first with isoflurane in 0.4 L/min O_2 and 0.6 L/min N_2O during catheterization, followed by isoflurane in 1.0 L/min medical air during ultrasound exposure to avoid shortening circulation time of the microbubbles. 50 µl of IRDye800CW-PEG (final concentration of 5 pmol/g body weight) or 50 µl of CCPM solution (final Cy7 dosage of 2 nmol Cy7 equiv. per animal) was injected intravenously. Mice to be treated with ACT received a bolus injection of 50 µl of microclusters (PS101) prior to 45-sec activation ultrasound and 300-sec enhancement ultrasound. This treatment was given 3 times within approximately 18 min. The ultrasound parameters used for activation and enhancement

are given in Table 2 and were based on previous work [27]. These parameters were found to improve the therapeutic response of various drugs without side effects. Two mechanical indexes (MI) of 0.2 or 0.3 for the enhancement step were used. Control mice received 3 times 50 µl saline instead of microclusters.

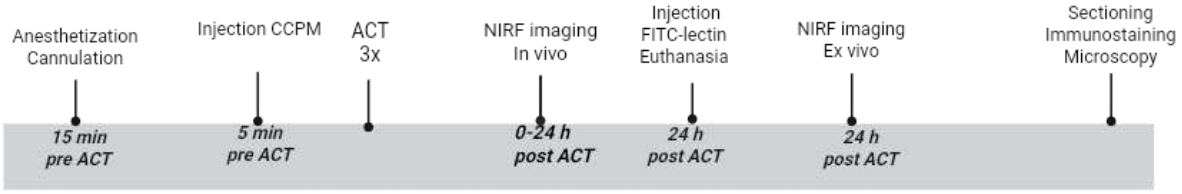

Figure 2. Timeline for the experimental procedure for CCPM. CCPMs were injected within 5 min before ACT. Tumour accumulation of CCPM was measured at various time points using Near Infrared Fluorescence (NIRF) imager. Before euthanasia, FITC-lectin was injected intravenously to label functional vessels. Tumour accumulation of CCPM was measured *ex vivo.* The microdistribution of CCPM, functional blood vessels, and collagen was assessed by confocal laser scanning microscopy (CLSM) and second-harmonic generation (SHG) imaging.

Table 2. Ultrasound parameters used for ACT

	ACT Activation (45 sec)	**ACT Enhancement (300 sec)**	
Frequency	2.7 MHz	0.5 MHz	0.5 MHz
Peak Negative Pressure (PNP)	0.49 MPa	0.15 MPa	0.21 MPa
Mechanical index (MI)	~0.3	~0.2	~0.3
Number of cycles	8	2	2
Pulse Repetition Frequency (PRF)	1 kHz	1 kHz	1 kHz

Near-infrared fluorescence imaging of CCPM and IRDye800CW-PEG uptake

To study the accumulation of CCPM in KPC tumours, the mice were placed in a NIRF imager and imaged *in vivo* 30 min, 1 hr, 2 hr and 24 hr as well as *ex vivo* 24 hr after ACT. IRDye800CW-PEG was imaged *in vivo* up to 2 hr after ACT. CCPM were excited at 675 nm, and fluorescence detected at 720 nm. IRDye800CW-PEG was excited at 745 nm and fluorescence emission was detected at 800 nm.

***In vivo* staining of functional vessels and sectioning of tumours**

Five min before euthanising the mice by cervical dislocation, the functional vessels were labelled by an intravenous injection of 50 µl fluorescein (FITC) labelled Lycopersicon esculentum tomato lectin (2 mg/ml, Vector Laboratories). The mice were anaesthesia using 2-3 % isoflurane in 0.4 L/min O_2 and 0.6 L/min N_2O during the injection and cervical dislocation.

For microscopy, tumours were mounted on a piece of cork with OCT Tissue Tek (Sakura) and submerged slowly in liquid nitrogen before 8 µm frozen sections were prepared.

Immunostaining of vessels

Total amount of blood vessels was imaged after immunostaining. Frozen tumour sections were fixed for 10 min in cold (-20 °C) acetone. Blocking of non-specific antibody binding was done by incubating the sections in 12 % bovine serum albumin (BSA) in PBS for 1 hr. Rat anti-mouse CD31 antibody (BD Bioscience) was diluted in PBS with 12 % BSA to 10 µg/ml and incubated at room temperature for 1 hr, followed by washing in PBS. The secondary donkey anti-rat IgG-AlexaFluor647 antibody (Jackson Immuno Research Labs) was diluted in PBS with 12 % BSA to 30 µg/ml and incubated at room temperature for 1 hour, followed by washing in PBS and mounting using Vectashield (Vector Laboratories).

Confocal laser scanning microscopy of tumour sections

Microdistribution of the CCPM was imaged by CLSM using a Leica SP8 SMD/MP Confocal Microscope and an HC PL APO 20x dry objective with a numerical aperture of 0.75. A total of 8 images were acquired in one tumour section for each tumour, 4 from the central region and 4 from the peripheral region. The Rhodamine B labelled CCPM were excited at 561 nm and fluorescence emission detected 570 - 700 nm. Functional blood vessels were labelled *in vivo* with FITC-labelled lectin which was excited at 488 nm and fluorescence detected at 495-540 nm. All blood vessels in the tumour section which were labelled with anti-CD31 and AlexaFluor 647 were excited at 640 nm and fluorescence detected at 656-700 nm.

Collagen imaging by the second harmonics generated (SHG) signal

The distribution of collagen in frozen sections was imaged by the second-harmonic generated (SHG) signal [34]. A titanium-sapphire (Ti: Sp) Chameleon Vision-S two-photon laser (Coherent) at 890 nm mounted on the Leica SP8 CLSM was used. The SHG signal was detected both in forward and backward directions. An emission filter of 445 ± 10 nm was placed in front of the two detectors. An air objective of 20X with a numerical aperture of 0.75 was used.

SHG is a scattering process in which two incoming photons of the same wavelength are scattered by non-centrosymmetric structures, like collagen fibres, into one photon of exactly half the wavelength [35, 36]. The resulting emission is coherent. Therefore, the directionality and intensity of the emitted light are sensitive to the microscopic properties of the fibrils and fibres scattering the light. The forward/backward SHG signal (F/B-ratio) is sensitive to properties of the collagen fibres such as fibril diameter, spatial extent of the scatters along the optical axis in collagen fibres and the extent of order in fibril packing [37]. More ordered collagen fibres will

have a stronger SHG signal in the forward direction, whereas chaotic collagen fibres have a stronger backscatter signal.

Histology

Frozen sections were stained with Hematoxylin-Erythrosin-Safran (HES). To assess tissue damage, tile scans of HES sections were imaged using a Zeiss LSM 800 and a 20x/0.8 Plan-Apochromat air objective and Axiocam 503 CCD camera. The HES sections were evaluated by a senior neuropathologist.

Image analysis

CCPM and IRDye800CW-PEG accumulation in tumours

From the NIRF images *in vivo*, Regions of Interest (ROI)s were drawn around the tumour as well as the muscle tissue in the untreated leg and Total Radiant Efficiency [p/s]/[μW/cm²] was measured using the Living Image software (v. 4.7.4; PerkinElmer). The tumour uptake is presented as Total Radiant Efficiency of CCPM or IRDye800CW-PEG divided by Total Radiant Efficiency for the muscle.

For the *ex vivo* measurements, ROIs were drawn around the tumour using the Auto ROI tool in the Living Image software. The Total Radiant Efficiency [p/s] / [μW/cm²] was measured for each tumour and normalized by tumour weight.

Extravasated CCPM estimated from CLSM images

The extravasated CCPM was estimated from CLSM images based on the number of pixels corresponding to the fluorescent CCPM. To identify the intravascular CCPM, the CCPM channel was colocalised with the functional vasculature channel by a vascular mask. The intravascular CCPM was excluded, and only extravascular CCPM included.

Functional vessels and collagen

CLSM images were analysed using ImageJ (version 1.51j). The Otsu thresholding algorithm was applied to segment the images, and the number of FITC-positive pixels was quantified across all images from each tumour section to estimate the abundance of functional blood vessels. Similarly, the number of pixels exhibiting forward-directed SHG signal was quantified across all images from each tumour section to assess the abundance of fibrillar collagen. The SHG F/B-ratio was based on signal intensities and the forward SHG signal was divided by the backward signal pixel-by-pixel.

Statistics

Statistical analysis was performed using GraphPad Prism (v8.0). The statistical test is specified in the caption of the corresponding figures. A p-value less than 0.05 was considered statistically significant.

Results

Tumour accumulation of CCPM and IRDye800CW-PEG

Tumour accumulation of CCPM up to 24 hours after administration of CCPM in control and ACT tumours is shown in Figure 3a. The results indicate a trend towards an increased accumulation of CCPM over time in both control and ACT tumours. There was no statistically significant difference between CCPM uptake in ACT and control tumours. The *ex vivo* quantification of the CCPM accumulation after 24 hours (Figure 3b) confirmed no statically significant uptake of CCPM in KPC tumours. CLSM images estimating the CCPM uptake extravascular were consistent with the NIFR images (Supplementary Figure S1).

We have previously demonstrated that ACT enhances the accumulation of IRDye800CW-PEG in subcutaneously growing prostate tumours in athymic mice [38]. Similar results were obtained in the present study. In KPC tumours, ACT increased the accumulation of IRDyeCW800-PEG by 1.5-fold over the 2-hour measurement period (Figure 3c).

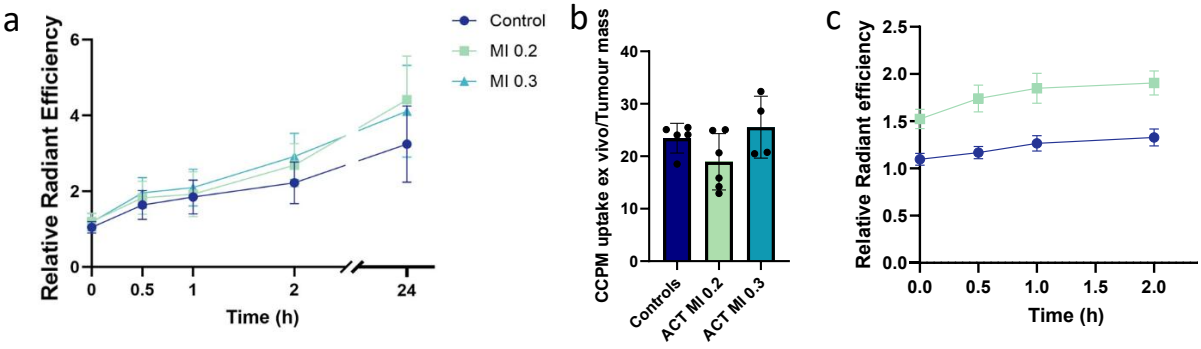

Figure 3: Accumulation of CCPM and IRDye800CW-PEG in KPC tumours. (a) Radiant efficiency of CCPM ((p/s)/(μW/cm^2)x10^8) in the tumour relative to control leg as a function of time after ACT. Mean with error bars indicating SD n=5-6 tumours per group. (b) *Ex vivo* accumulation of CCPM (total radiant efficiency (p/s)/(μW/cm^2)x10^8/mg) for control tumours and ACT tumours 24 h after ACT. Each symbol represents one tumour. (c) Radiant efficiency of IRDye800CW-PEG in tumour relative to control leg as a function of time after ACT. Mean with error bars indicating SD, n=5-6 tumours per group.

Microdistribution of CCPM in tumours

Representative CLSM images showing the microdistribution of CCPM in KPC tumours 24 hr after intravenous injection in control and ACT mice are shown in Figure 4. The CLSM images revealed that both control and ACT tumours contained high levels of CCPM both in the periphery and central part of the tumours.

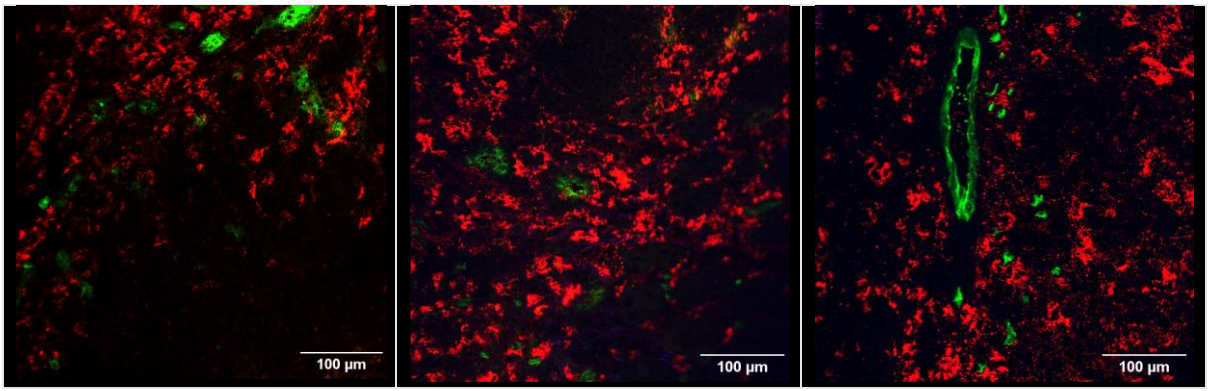

Figure 4. Representative CLSM images showing the microdistribution of CCPM in KPC tumours 24 hours after intravenous injection. (a) Control mice. (b) ACT tumour at MI of 0.2 and (c) MI of 0.3 for enhancement step. CCPM are displayed in red and lectin-FITC-labelled vessels in green. The scale bars represent 100 µm.

Tumour microenvironment

Histopathology

The HES-stained sections (Figure 5) show that the KPC tumours are poorly differentiated with necrotic areas in the core and infiltrated muscle tissue in the periphery. The tumours display quite low amounts of connective tissue, indicating less extensive desmoplasia. Granulocytes were observed within the tumour in the control and ACT groups.

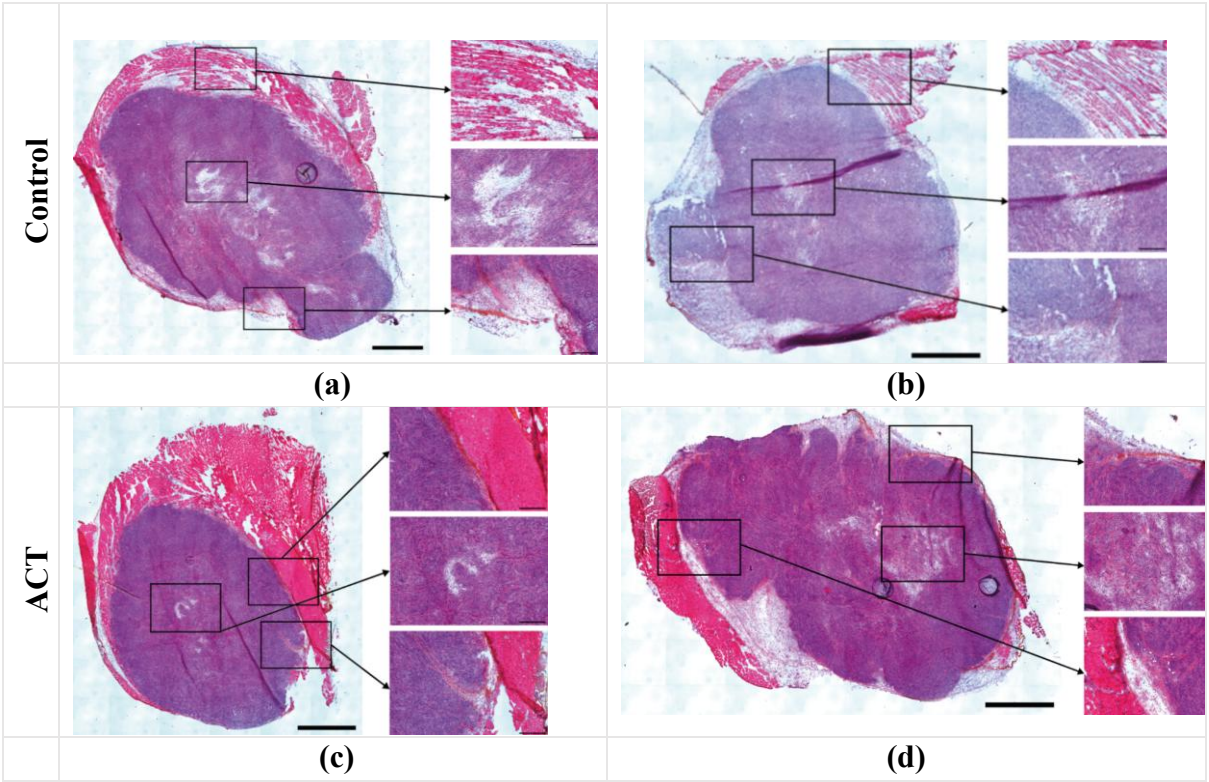

Figure 5. HES stained frozen tumour sections. (a,b) control tumours. (c,d) ACT tumors. Three zoom areas show the periphery of the tumour (upper), necrosis in the central part (middle) and the interface between the tumour and muscle tissue (lower). The scale bar is 100 µm.

Variation in vasculature

A large variation in the number of functional blood vessels and the total number of blood vessels was observed within tumour sections and between sections from different tumours. Representative examples of CLSM images of control and ACT tumours are shown in Supplementary (Figure S2). The well vascularised tumours showed little necrosis, whereas in the tumours with few vessels in the central part necrosis was observed, which is consistent with the HES sections (Figure 5).

Extracellular matrix – Amount and organization of the collagen network

Fibrillar collagen networks in the extracellular matrix are reported to limit the penetration of NPs [39]. Fibrillar collagen was therefore imaged by the SHG signal. Figure 6 shows images of the collagen network (blue forward direction and magenta backward direction) and accumulation of CCPM (red). Blood vessels are shown in green. The CCPM seemed to be located in the perifery of the collagen network in control tumours (Figure 6 a,b) and infiltrating the collagen network to a larger extent in ACT tumours (Figure 6 c,d).

A quantitative analysis of the amount of collagen and orientation of the collagen fibres is shown Figure 7. The number of pixels with an SHG signal indicates the amount of collagen fibres, and the ratio of SHG intensity in forward and backward direction represents fibre orientation and the organisation of the collagen network.

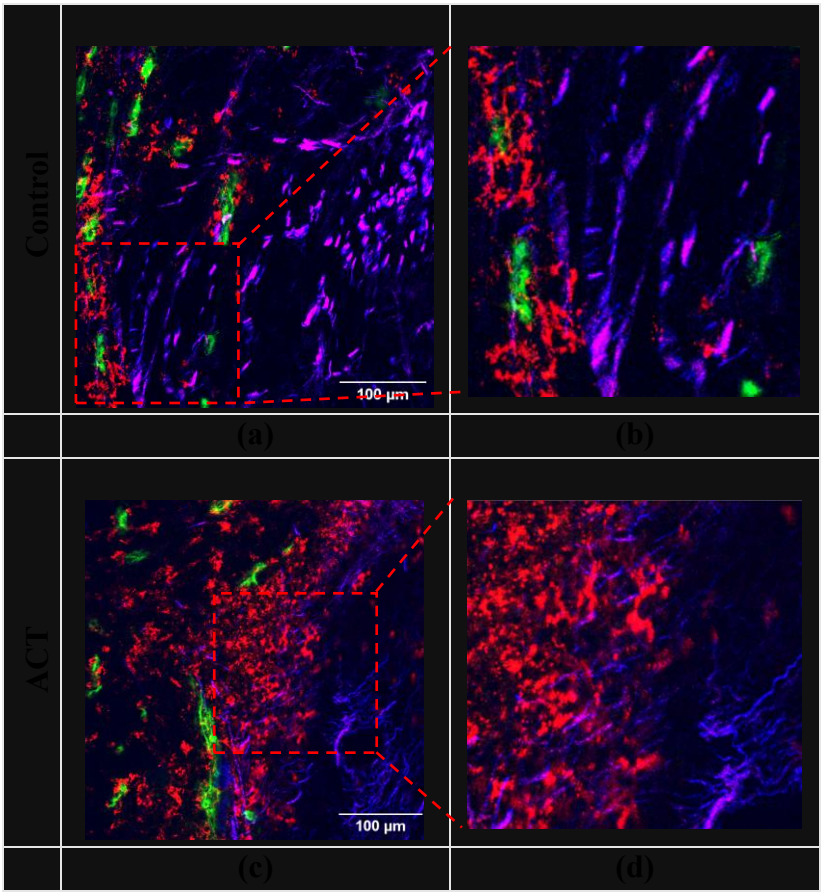

Figure 6. Fibrillar collagen imaged by SHG signal in forward (blue) and backward direction (magenta), functional blood vessels (green) and CCPM (red). (a) Representative image of control and (c) ACT tumours and (b, d) zoomed-in view images.

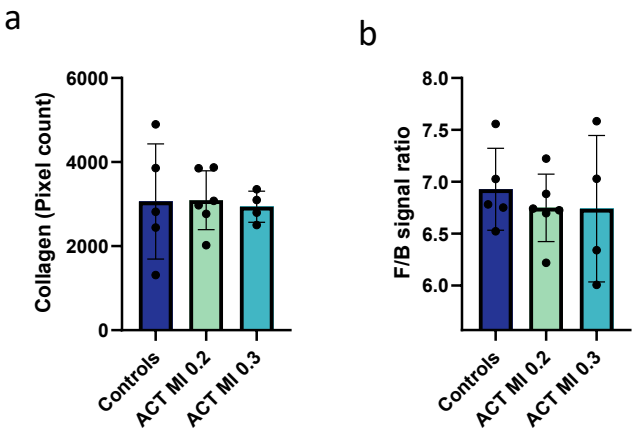

Figure 7. Quantitative analysis of collagen fibres imaged by SHG signals in control and ACT tumours. (a) Total amount of SHG signal. (b) F/B-intensity ratio, n=4-6 tumours per group. Data are displayed as mean with error bars indicating SD. Each symbol represents one tumour.

ACT had no detectable effects on neither the amount of collagen nor the F/B-ratio of the SHG signal within the time frame and spatial resolution of SHG microscopy. The SHG signal was averaged over 8 different images in each tumour section, 4 images in the periphery and 4 images in the central part of the tumour.

Potential causes for the observed variation in the accumulation of CCPM in KPC tumours

To obtain information on tumour properties that may cause the variation in CCPM uptake, the *ex vivo* uptake of CCPM was correlated with the amount of functional blood vessels, amount of collagen and F/B-SHG signal, and tumour weight, all parameters measured on individual tumours 24 hours after ACT.

ACT had no effect on the number of functional vessels (Figure 8 a), and no correlation was found between the uptake of CCPM *ex vivo* normalised to tumour mass and displayed as a function of number of functional vessels (Figure 8 b).

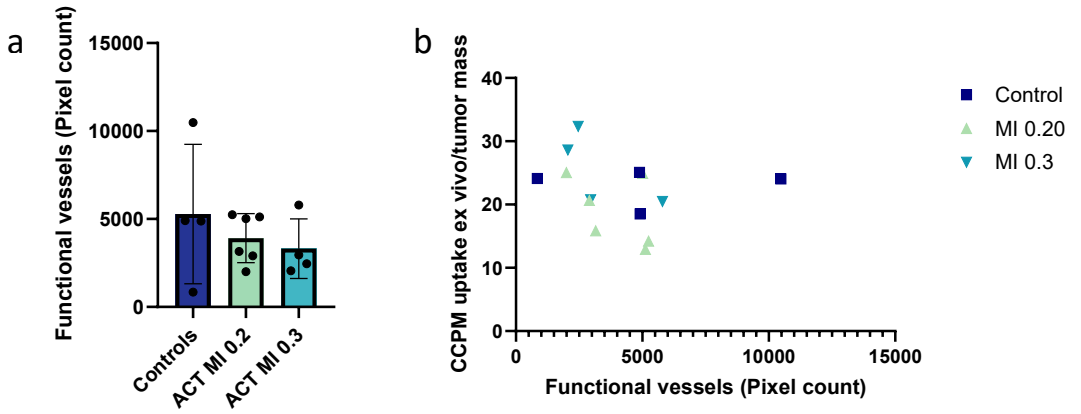

Figure 8. Functional blood vessels and tumour uptake of CCPM in control and ACT tumours. (a) Amount of functional vessels. Mean with error bars indicating SD, n=4-6 tumours per group. (b) *Ex vivo* tumour uptake of CCPM per tumour mass versus amount of functional vessels. CCMP uptake expressed as total radiant efficiency (p/s)/(μW/cm^2)x10^8/mg. Each symbol represents one tumour.

Tumour uptake of CCPM *ex vivo* normalised to tumour mass showed no correlation with collagen content (Figure 9a). However, a positive correlation was observed between tumour uptake of CCPM and the F/B-ratio of SHG intensity (Figure 9b). This correlation was statistically significant when all data were pooled, as indicated by the solid line in Figure 9b (p = 0.011). When the ACT tumours were analysed separately, the correlation was statistically significant in the MI 0.2 group (p = 0.025), but not in the MI 0.3 group (p = 0.090).

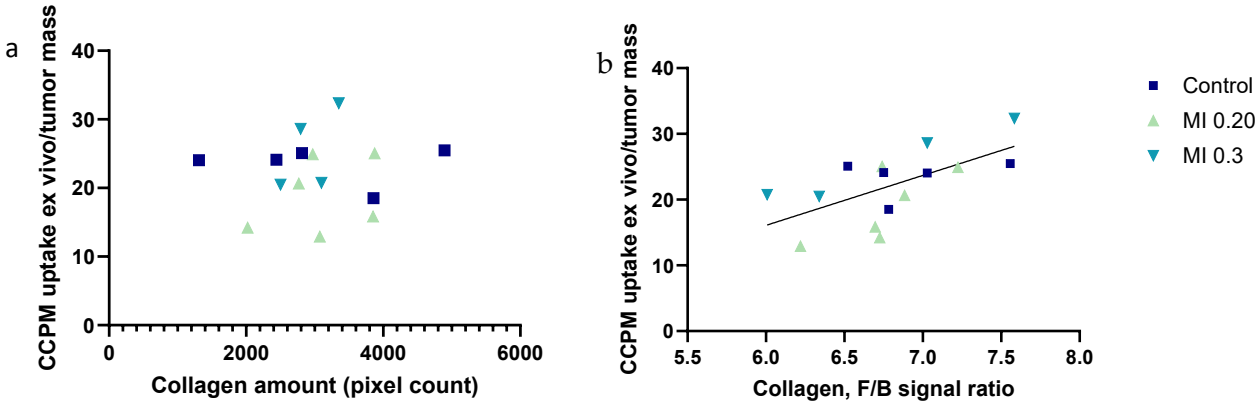

Figure 9. *Ex vivo* tumour uptake of CCPM per tumour mass and collagen in control and ACT tumours. (a) *Ex vivo* tumour uptake of CCPM as a function of amount of collagen measured as the number of pixels with SHG signal in the forward direction. (b) *Ex vivo* tumour uptake of CCPM as a function of F/B-ratio of the SHG signal intensity. CCMP uptake expressed as total radiant efficiency (p/s)/(μW/cm^2)x10^8/mg. The solid line represents the statistically significant regression curve (p=0.011). Each symbol represents one tumour, n=4-6 animals per group.

The weight of the tumours ranged from 50 to 220 mg. Within such a small range of tumour weights, no correlation with the uptake of CCPM was found, neither in the control nor in ACT tumours (Figure 10).

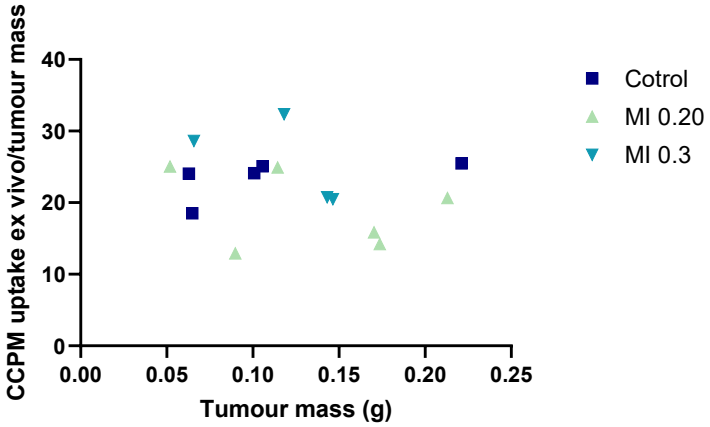

Figure 10. *Ex vivo* tumour uptake of CCPM as a function of tumour mass in control and ACT tumours. CCMP uptake expressed as total radiant efficiency (p/s)/(μW/cm^2)x10^8/mg. Each symbol represents one tumour, with n=4-6 animals per group.

Discussion

A prerequisite for successful cancer chemotherapy is that the therapeutic agent accumulates within the tumour and reaches the tumour cells. ACT has previously been shown to improve the efficacy of several co-injected chemotherapeutic agents in xenograft mouse models of prostate cancer [27], triple-negative breast cancer [28], colon cancer [40] and PDAC [41]. However, the therapeutic response varies both between tumour types and among tumours of the same type. This variability is not unique to ACT but represents a general challenge in cancer treatment, observed in preclinical animal models and in patients receiving a wide range of therapeutic agents, either alone or in combination with other treatment modalities, including ultrasound-mediated drug delivery. Understanding the factors underlying this variability is therefore essential for identifying patients most likely to benefit from ultrasound-mediated drug delivery. Here, we aimed to identify characteristics of the tumour microenvironment that may influence the accumulation of co-injected CCPM in a PDAC model derived from genetically engineered KPC mice.

ACT efficacy depends on cargo properties and baseline tumour uptake

A key finding is the different response of CCPM and IRDye800CW-PEG to ACT-mediated delivery. While ACT increased tumour accumulation of the macromolecule IRDye800CW-PEG by approximately 50 %, the enhancement of CCPM uptake was not statistically significant. The uptake of CCPM into KPC tumours was high, and CCPM displayed a more homogeneous distribution throughout the tumour compared to what we have seen previously for liposomes and polymeric NPs in prostate xenografts [42, 43]. The high tumour uptake may be due to the long systemic circulation of CCPM, which was 16 hours in rats [10], in combination with a potentially efficient EPR effect. Applying machine-learning-assistant analysis of vascular permeability of small NPs in 32 tumours, several of the PDACs analysed were found to have a very high vascular permeability [7]. We have previously found efficient uptake of IRDye800CW-PEG in the KPC tumour model in the absence of ACT, indicating

hyperpermeable tumour vessels in the KPC tumour model [44]. Furthermore, the diameter of the CCPM was 65 nm, which could be advantageous for extravasation and penetration throughout the extracellular matrix, as compared to the larger NPs with diameters of 100-200 nm [42, 43]. The charge of the molecules moving across the negatively charged endothelium and extracellular matrix is another factor important for drug delivery [45]. CCPM is reported to be neutral with a zetapotential between -2 and 0 mV [10] whereas the liposomes and polymeric NPs previously used were negatively charged, respectively -15 mV and -3 mV [42, 43]. A diameter of 65 nm and neutral charge combined with highly permeable capillaries, can explain the high uptake and well distributed CCPM in control tumours. This efficient tumour uptake may limit further enhancement and can explain why ACT did not have any additional effect.

In contrast, ACT significantly increased tumour uptake of the macromolecule IRDye800CW-PEG. IRDye 800CW-PEG is designed to exploit the EPR effect and diffuse into tumour tissue, making this macromolecule a widely used tool in tumour imaging in preclinical studies [46, 47]. Several physicochemical properties that may influence tumour uptake differ between CCPM and IRDye800CW-PEG, including size, structure, and surface charge. CCPM has a hydrodynamic diameter of approximately 65 nm, compared with approximately 12 nm for IRDye800CW-PEG. Furthermore, whereas IRDye800CW-PEG is a flexible, random-coil macromolecule, CCPM has a more compact structure. The two agents differ in surface charge: CCPM has a zetapotential ranging from −2 to 0 mV (10), whereas IRDye800CW-PEG is negatively charged, with a zeta potential ranging from −11 to −17 mV. Although these differences may influence how the two agents interact with the tumour microenvironment, it remains unclear which properties, or combination of properties, account for the observed differences in ACT-mediated tumour delivery.

Tumour microenvironment determines the uptake of NPs and effect of ACT

Considerable inter-tumour variability in CCPM accumulation was observed in both untreated control and ACT tumours. To identify potential determinants of this variability, we examined the effect of ACT on tumour microenvironmental parameters.

ACT had no effect on the number of functional vessels 24 hours after ACT. However, potential changes in perfusion may have been restored after 24 hours [48]. In a previous study, we compared the effect of ultrasound plus the microbubble SonoVue and ACT on number of functional vessels in four different tumour models including the KPC model. Immediately after ultrasound and SonoVue the number of functional vessels was reduced in the breast and colon tumour models, but not in the KPC model. ACT had no effect on functional vessels in neither the KPC nor the colon tumour model [48]. The difference between ACT and ultrasound plus SonoVue may be that the ultrasound pressure and pulse length are smaller for ACT compared to ultrasound and SonoVue treatment and the number of ACT bubbles is less than the number of oscillating SonoVue bubbles.

No correlation between uptake of CCPM and functional vessels was found, when pooling all measurements in treated and untreated tumours together. This may suggest that the delivery is

not governed solely by the extent of perfused vasculature. During ACT, only a small fraction of the capillaries contain activated ACT bubbles [24, 32]. As ACT bubbles are present in fewer capillaries, the fraction of functional vessels may not be a critical parameter for efficient delivery of drugs in combination with ACT.

The amount and the organisation of collagen fibres were measured by the SHG signal. The F/B-ratio of the SHG signal reflects the collagen structure and alignment, and a high ratio indicates more aligned collagen fibres, with a stronger forward-propagating SHG signal than the backwards-propagating signal. We could not detect any changes in either the amount or the structure/ordering of the collagen fibrils after ACT. Any changes most likely occur close to the vessel wall where the ACT bubbles oscillate. However, as we have no information on ACT bubble location, imaging in the proximity of oscillating bubbles was not possible. The SHG signals were averaged from 8 regions of the tumour sections, and any local change could not be detected.

Importantly, we found that the tumour uptake of CCPM increased with increasing F/B-ratio demonstrating that alignment of collagen fibres facilitates the uptake of CCPM. This is consistent with several studies demonstrating that ordered and aligned collagen fibres in tumours improve drug diffusion and uptake [49-51]. On the other hand, the uptake of CCPM did not depend on the amount of collagen as reported by others [52]. Torosean et al [52] compared the uptake of 40 nm NPs in three tumour models and the pancreatic tumour, which had the most collagen measured by Masson's Trichrome staining, showed the lowest uptake of the NPs.

Conclusion

Our findings demonstrate that delivery efficacy of ACT in the KPC model is influenced by both the physicochemical properties of the delivery cargo and the tumour microenvironment. ACT significantly enhanced tumour uptake of the rather small, flexible, and negatively charged macromolecular tracer IRDye800CW-PEG, whereas ACT did not increase the tumour uptake of the larger and electrically neutral CCPM. CCPM exhibited high accumulation and intratumoural distribution in control tumours, indicating that the KPC tumour capillaries are rather leaky and that the properties of CCPM are favourable for tumour accumulation. The high baseline accumulation of CCPM may explain why no additional uptake of CCPM was observed after ACT. Inter-tumour variability of CCPM uptake was not explained by amount of functional vessels or amount of collagen fibrils, but correlated with the alignment of collagen fibres, suggesting that tumours with a chaotic collagen network may be intrinsically less susceptible to NP accumulation and therapy. This study represents an initial step towards defining biomarkers for successful ultrasound-mediated drug delivery. The relatively small number of tumours analysed represents a limitation. However, our results highlight the need to consider both NP properties and tumour microenvironmental constraints, in particular organization of the collagen network, to achieve successful ACT-mediated delivery of NPs and ultrasound-mediated delivery in general.

Acknowledgement

The authors thank Yves Boucher and Nilesh P. Talele Mass General Hospita Boston, USA, for providing the KPC cell line. Thanks to GE Healthcare and EXACT Therapeutics for providing PS101. Thanks to Marieke Olsman for assisting during experiments. The animals were housed at the Comparative Medicine Core Facility (CoMed, NTNU), and tissue sections were prepared by the Cellular and Molecular Imaging Core Facility (CMIC, NTNU) and analysed at Center for Advanced Microscopy (CAM, NTNU). The IVIS measurements were performed at the MR Core Facility, NTNU. MR Core facility is funded by the Faculty of Medicine and Health Sciences at NTNU and Central Norway Regional Health Authority. The mechanical workshop at NTNU is acknowledged for making the water tank. Kenneth Andersen and Lars Hoff are acknowledged for designing and producing the dual-frequency transducer. Illustrations were created with BioRender.com. The work was supported by the Norwegian University of Science and Technology (NTNU, Trondheim, Norway) and the Research Council of Norway, grant number Nano2021 262228.

Author contribution: JLF, MM, SS, ES, AW, CJFR, QH, MT, CLD Study design; JLF, MM, CÅ, SS, ES, AW performed experiments and analyzed data together with CJFR, QH, MT, CLD; SHT analyzed HES sections; QH and MT prepared CCPM; JLF wrote first draft and CLD finished the manuscript. All authors commented on the manuscript. All authors approved the manuscript.

Data availability: All data supporting the findings of this study are available within the paper and its Supplementary Information.

Competing Interest Statement: The authors declare no competing interest. Melina Mühlenpfordt and Einar Sulheim are employed at EXACT Therapeutics AS. Employment of started after they conduction of the study.

References

1. Zhou, Y., Chen, X., Cao, J. & Gao, H. Overcoming the biological barriers in the tumor microenvironment for improving drug delivery and efficacy. *J Mater Chem B* **8**, 6765–6781 (2020).
2. Stylianopoulos, T., Munn, L.L. & Jain, R.K. Reengineering the Physical Microenvironment of Tumors to Improve Drug Delivery and Efficacy: From Mathematical Modeling to Bench to Bedside. *Trends in Cancer* **4**, 292–319 (2018).
3. Dewhirst, M.W. & Secomb, T.W. Transport of drugs from blood vessels to tumour tissue. *Nature Reviews Cancer* **17**, 738–750 (2017).
4. Ilic, M. & Ilic, I. Epidemiology of pancreatic cancer. *World J Gastroenterol* **22**, 9694–9705 (2016).
5. Khawar, I.A., Kim, J.H. & Kuh, H.J. Improving drug delivery to solid tumors: priming the tumor microenvironment. *J Control Release* **201**, 78–89 (2015).
6. Heinrich, M.A., Mostafa, A., Morton, J.P., Hawinkels, L. & Prakash, J. Translating complexity and heterogeneity of pancreatic tumor: 3D in vitro to in vivo models. *Adv Drug Deliv Rev* **174**, 265–293 (2021).
7. Zhu, M. et al. Machine-learning-assisted single-vessel analysis of nanoparticle permeability in tumour vasculatures. *Nature Nanotechnology* **18**, 657–666 (2023).

8. Rijcken, C.J.F. et al. Design, development and clinical translation of CriPec®-based core-crosslinked polymeric micelles. *Advanced Drug Delivery Reviews* **191**, 114613 (2022).
9. Talelli, M. et al. Core-Crosslinked Polymeric Micelles: Principles, Preparation, Biomedical Applications and Clinical Translation. *Nano Today* **10**, 93–117 (2015).
10. Hu, Q., Prakash, J., Rijcken, C.J., Hennink, W.E. & Storm, G. High systemic availability of core-crosslinked polymeric micelles after subcutaneous administration. *Int J Pharm* **514**, 112–120 (2016).
11. Hu, Q. et al. Complete regression of breast tumour with a single dose of docetaxel-entrapped core-cross-linked polymeric micelles. *Biomaterials* **53**, 370–378 (2015).
12. Atrafi, F. et al. A phase I dose-escalation and pharmacokinetic study of a micellar nanoparticle with entrapped docetaxel (CPC634) in patients with advanced solid tumours. *J Control Release* **325**, 191–197 (2020).
13. Wilhelm, S. et al. Analysis of nanoparticle delivery to tumours. *Nature Reviews Materials* **1**, 16014 (2016).
14. Dai, Q. et al. Quantifying the Ligand-Coated Nanoparticle Delivery to Cancer Cells in Solid Tumors. *ACS nano* **12**, 8423–8435 (2018).
15. Snipstad, S. et al. Sonopermeation Enhances Uptake and Therapeutic Effect of Free and Encapsulated Cabazitaxel. *Ultrasound Med Biol* **47**, 1319–1333 (2021).
16. Kotopoulis, S. et al. Sonoporation-enhanced chemotherapy significantly reduces primary tumour burden in an orthotopic pancreatic cancer xenograft. *Mol imaging biol* **16**, 53–62 (2014).
17. Haram, M. et al. Ultrasound and Microbubbles Increase the Uptake of Platinum in Murine Orthotopic Pancreatic Tumors. *Ultrasound Med Biol* **49**, 1275–1287 (2023).
18. Lin, C.Y., Li, J.R., Tseng, H.C., Wu, M.F. & Lin, W.L. Enhancement of focused ultrasound with microbubbles on the treatments of anticancer nanodrug in mouse tumors. *Nanomedicine* **8**, 900–907 (2012).
19. Bressand, D. et al. Enhancing Nab-Paclitaxel Delivery Using Microbubble-Assisted Ultrasound in a Pancreatic Cancer Model. *Molecular pharmaceutics* **16**, 3814–3822 (2019).
20. Han, F. et al. Clinical sonochemotherapy of inoperable pancreatic cancer using diagnostic ultrasound and microbubbles: a multicentre, open-label, randomised, controlled trial. *Eur Radiol* **34**, 1481–1492 (2024).
21. Dimcevski, G. et al. A human clinical trial using ultrasound and microbubbles to enhance gemcitabine treatment of inoperable pancreatic cancer. *J control release* **243**, 172–181 (2016).
22. Haram, M. et al. Treatment of inoperable pancreatic adenocarcinoma with focused ultrasound and microbubbles in patients receiving chemotherapy. *WFUMB Ultrasound Open* **3** (2025).
23. van Wamel, A. et al. Ultrafast Microscopy Imaging of Acoustic Cluster Therapy Bubbles: Activation and Oscillation. *Ultrasound Med Biol* **48**, 1840–1857 (2022).
24. Sontum, P. et al. Acoustic Cluster Therapy (ACT)--A novel concept for ultrasound mediated, targeted drug delivery. *Int J Pharm* **495**, 1019–1027 (2015).
25. Fernandez, J.L., Snipstad, S., Bjørkøy, A. & Davies, C.L. Real-Time Multiphoton Intravital Microscopy of Drug Extravasation in Tumours during Acoustic Cluster Therapy. *Cells* **13** (2024).
26. Mühlenpfordt, M. et al. Real-time Imaging of Vascular Changes and Extravasation in the Chicken Chorioallantoic Membrane (CAM) Model Exposed to Ultrasound and Microbubbles. *Ultrasound Med Biol* **51**, 1971–1983 (2025).

27. van Wamel, A. et al. Acoustic Cluster Therapy (ACT) enhances the therapeutic efficacy of paclitaxel and Abraxane(R) for treatment of human prostate adenocarcinoma in mice. *J control release* **236**, 15–21 (2016).
28. Bush, N. et al. Theranostic Attributes of Acoustic Cluster Therapy and Its Use for Enhancing the Effectiveness of Liposomal Doxorubicin Treatment of Human Triple Negative Breast Cancer in Mice. *Front Pharmacol* **11**, 75 (2020).
29. Ng, S. et al. Effect of acoustic cluster therapy (ACT(R)) combined with chemotherapy in a patient-derived xenograft mouse model of pancreatic cancer. *J control release* **352**, 1134–1143 (2022).
30. Stylianopoulos, T., Diop-Frimpong, B., Munn, L.L. & Jain, R.K. Diffusion anisotropy in collagen gels and tumors: the effect of fiber network orientation. *Biophys J* **99**, 3119–3128 (2010).
31. Hu, Q. et al. Tailoring the physicochemical properties of core-crosslinked polymeric micelles for pharmaceutical applications. *J control release* **244**, 314–325 (2016).
32. Healey, A.J. et al. Acoustic Cluster Therapy: In Vitro and Ex Vivo Measurement of Activated Bubble Size Distribution and Temporal Dynamics. *Ultrasound Med Biol* **42**, 1145–1166 (2016).
33. Andersen, K.K., Healey, A., Bush, N.L., Frijlink, M.E. & Hoff, L. A Harmonic Dual-Frequency Transducer for Acoustic Cluster Therapy. *Ultrasound Med Biol* **45**, 2381–2390 (2019).
34. Erikson, A., Ortegren, J., Hompland, T., de Lange Davies, C. & Lindgren, M. Quantification of the second-order nonlinear susceptibility of collagen I using a laser scanning microscope. *J Biomed Opt* **12**, 044002 (2007).
35. Chen, X., Nadiarynkh, O., Plotnikov, S. & Campagnola, P.J. Second harmonic generation microscopy for quantitative analysis of collagen fibrillar structure. *Nature Protocols* **7**, 654–669 (2012).
36. Campagnola, P.J. & Loew, L.M. Second-harmonic imaging microscopy for visualizing biomolecular arrays in cells, tissues and organisms. *Nature Biotechnology* **21**, 1356–1360 (2003).
37. Williams, R.M., Zipfel, W.R. & Webb, W.W. Interpreting second-harmonic generation images of collagen I fibrils. *Biophysical J* **88**, 1377–1386 (2005).
38. Wamel, A.V. et al. Acoustic Cluster Therapy (ACT) - pre-clinical proof of principle for local drug delivery and enhanced uptake. *J control release* **224**, 158–164 (2016).
39. Eikenes, L., Bruland, O.S., Brekken, C. & Davies Cde, L. Collagenase increases the transcapillary pressure gradient and improves the uptake and distribution of monoclonal antibodies in human osteosarcoma xenografts. *Cancer research* **64**, 4768–4773 (2004).
40. Bush, N. et al. Therapeutic Dose Response of Acoustic Cluster Therapy in Combination With Irinotecan for the Treatment of Human Colon Cancer in Mice. *Front Pharmacol* **10**, 1299 (2019).
41. Ng, S. et al. Effect of acoustic cluster therapy (ACT®) combined with chemotherapy in a patient-derived xenograft mouse model of pancreatic cancer. *J Control Release* **352**, 1134–1143 (2022).
42. Olsman, M. et al. Ultrasound-mediated delivery enhances therapeutic efficacy of MMP sensitive liposomes. *J control release* **325**, 121–134 (2020).
43. Sulheim, E. et al. Sonopermeation with Nanoparticle-Stabilized Microbubbles Reduces Solid Stress and Improves Nanomedicine Delivery to Tumors. *Advanced Therapeutics* **4**, 2100147 (2021).

44. Fernandez, J.L. et al. A Comparative Analysis of Orthotopic and Subcutaneous Pancreatic Tumour Models: Tumour Microenvironment and Drug Delivery. *Cancers (Basel)* **15** (2023).
45. Stylianopoulos, T. et al. Diffusion of Particles in the Extracellular Matrix: The Effect of Repulsive Electrostatic Interactions. *Biophysical J* **99**, 1342–1349 (2010).
46. Llaguno-Munive, M., Villalba-Abascal, W., Aviles-Salas, A. & Garcia-Lopez, P. Near-Infrared Fluorescence Imaging in Preclinical Models of Glioblastoma. *J Imaging* **9** (2023).
47. Knopf, P. et al. Preclinical Identification Of Tumor-Draining Lymph Nodes Using a Multimodal Non-invasive In vivo Imaging Approach. *Mol Imaging Biol* **25**, 606–618 (2023).
48. Snipstad, S. et al. Ultrasound and Microbubble-Induced Reduction of Functional Vasculature Depends on the Microbubble, Tumor Type and Time After Treatment. *Ultrasound Med Biol* **51**, 33–42 (2025).
49. Leddy, H.A., Haider, M.A. & Guilak, F. Diffusional anisotropy in collagenous tissues: fluorescence imaging of continuous point photobleaching. *Biophys J* **91**, 311–316 (2006).
50. Chen, X. et al. Glycosaminoglycans modulate long-range mechanical communication between cells in collagen networks. *Proc Natl Acad Sci U S A* **119**, e2116718119 (2022).
51. He, X. et al. Extracellular matrix physical properties govern the diffusion of nanoparticles in tumor microenvironment. *Proc Natl Acad Sci USA* **120**, e2209260120 (2023).
52. Torosean, S. et al. Nanoparticle uptake in tumors is mediated by the interplay of vascular and collagen density with interstitial pressure. *Nanomedicine: Nanotechnology, Biol Med* **9**, 151–158 (2013).

Supplementary Files

This is a list of supplementary files associated with this preprint. Click to download.

- Supplementary.docx
- Sourcedatafigure78910.xlsx